ADVANCED FUNCTIONAL MATERIALS
www.afm-journal.de



# Transparent and Flexible Inorganic Perovskite Photonic Artificial Synapses with Dual-Mode Operation

*Lin Yang, Mriganka Singh, Shin-Wei Shen, Ke-Yun Chih, Shun-Wei Liu, Chih-I Wu, Chih-Wei Chu,* and Hao-Wu Lin**

**With the rapid development of artificial intelligence, the simulation of the human brain for neuromorphic computing has demonstrated unprecedented progress. Photonic artificial synapses are strongly desirable owing to their higher neuron selectivity, lower crosstalk, wavelength multiplexing capabilities, and low operating power compared to their electric counterparts. This study demonstrates a highly transparent and flexible artificial synapse with a two-terminal architecture that emulates photonic synaptic functionalities. This optically triggered artificial synapse exhibits clear synaptic characteristics such as paired-pulse facilitation, short/long-term memory, and synaptic behavior analogous to that of the iris in the human eye. Ultraviolet light illumination-induced neuromorphic characteristics exhibited by the synapse are attributed to carrier trapping and detrapping in the $SnO_2$ nanoparticles and $CsPbCl_3$ perovskite interface. Moreover, the ability to detect deep red light without changes in synaptic behavior indicates the potential for dual-mode operation. This study establishes a novel two-terminal architecture for highly transparent and flexible photonic artificial synapse that can help facilitate higher integration density of transparent 3D stacking memristors, and make it possible to approach optical learning, memory, computing, and visual recognition.**

## 1. Introduction

The impending end of Moore's Law has resulted in scientists rethinking the approach to computing.[1] Given the constraints of the von Neumann bottleneck, an in-memory computing memristor has been considered a solution to brain-inspired neuromorphic computing, which imitates principles of biological synapses in a large network of neurons; this has emerged as a promising approach for developing exceptionally energy-efficient, time-efficient, and fault-tolerant computing technologies.[2] Memristors mimic the functions of biological synapses using a storage layer that can be reconfigured dynamically under consecutive external stimuli such as through electric fields,[3] magnetic fields,[4] or light illumination,[5] and this leads to variations in local conductivity and memory effects. With the rapid development of artificial intelligence, all-electronic memristors are being widely explored in current published approaches.[6–8] Another alternative solution is using a photonic system.[9–11] The combination of optical memristors and photonic computing can lead to a new era of self-learning computing systems. Recently, the device properties of photonic artificial synapses were investigated owing to their advantages such as high neuron selectivity, low crosstalk, wavelength multiplexing capabilities, and low operating power.[12–15] Previous literatures on photonic artificial synapses have demonstrated transparent[11,16] or flexible[5,17] devices. Perovskite-based photonic synapses have also been explored recently.[9,18–20] However, the simultaneous properties of transparency and flexibility, which are mainly limited by the structure and optical properties, have not been explored yet. Few two-terminal memristors that employ optical methods have been reported thus far.[21] The structure of a three-terminal device limits scalability and integration density, whereas the two-terminal device is structurally closer to biological neurons and allows lateral integration. Two-terminal photonic memristors enable on-chip optical interconnections that can substitute electric wires for connecting memories;[22] further, they show greater feasibility for vertical integration,[23] which can achieve an extremely high density on processor chips[24] and directly sense the desired image without a second transformation of the electric signals.[25] Furthermore, because the biological nerve system has a 3D form, the two-terminal architecture is considered a promising candidate for a 3D stacking memristor,[26] as it can achieve high densities, similar to the human cerebral cortex ($\approx 10^{15}$ synapses).[27]

Light is crucial not only for image formation but also for regulating many neurobehavioral functions.[28] Although the

L. Yang, Prof. H.-W. Lin
Department of Materials Science and Engineering
National Tsing Hua University
Hsinchu 30013, Taiwan
E-mail: hwlin@mx.nthu.edu.tw
Dr. M. Singh, Prof. C.-W. Chu
Research Center for Applied Sciences
Academia Sinica
Taipei 11529, Taiwan
E-mail: gchu@gate.sinica.edu.tw
S.-W. Shen, Prof. C.-I. Wu
Graduate Institute of Photonics and Optoelectronics
National Taiwan University
Taipei 10617, Taiwan
K.-Y. Chih, Prof. S.-W. Liu
Department of Electronic Engineering
Ming Chi University of Technology
New Taipei City 24301, Taiwan
The ORCID identification number(s) for the author(s) of this article can be found under https://doi.org/10.1002/adfm.202008259.

DOI: 10.1002/adfm.202008259

 

human retina cannot detect ultraviolet (UV)-light,[11] it can largely increase the cognitive activity of the brain, including the left hippocampus, left thalamus, and right amygdala, which are closely related to memory.[29,30] Inorganic $CsPbCl_3$ perovskite is considerably sensitive to UV light and extremely stable;[31] further, the low phase transition temperature below 50 °C[32] is also suitable for flexible device fabrication. However, owing to the poor solubility of its precursor,[33] the potential of this material as an optical memristor has not been explored so far. In this study, we use a vacuum-deposition method to yield a transparent and flexible artificial photonic synapse with low-temperature-processed UV-light absorber. The characteristics of $CsPbCl_3$-based light-driven artificial synapse device with a two-terminal structure and its synaptic functions mimicking biological memory are comprehensively investigated. The increase in photoconductivity after repeated light spikes is attributed to carrier trapping and detrapping in the device interfaces. The ability to detect deep red light is also observed, showing the potential of dual-mode operation in our devices. Our work establishes a novel architecture for photonic artificial synapse, and demonstrates the learning properties tuned by the UV light of the devices that imitate the human visual and memory system.

## 2. Results and Discussion

Nerve cells communicate through an interconnected network of neurons, which transmit chemical and electrical signals to facilitate communication between the brain and the body. A synapse is a two-terminal structure that permits communication between two neurons or a target cell, and it allows the rapid transmission of nerve impulses to other cells. The nerve impulses pass the chemical and electrical signals from the presynaptic (sending) neuron and postsynaptic (receiving) neuron, as illustrated in **Figure 1**a. Most neuromorphic devices utilize electrical signals to provide action potentials to emulate neural or synaptic behavior. Compared to electrical stimulation, optical pulses have advantages such as higher neuron selectivity, higher bandwidth, and low power consumption.[16,34–36] Hence, in this study, photonic signals are explored as the action potential to emulate several important synaptic functions in the two-terminal $CsPbCl_3$ synaptic devices, which have a structure similar to a synapse of the biological neural system.

The two-terminal devices with the vertical architecture of ITO/$SnO_2$/$CsPbCl_3$/TAPC/TAPC:$MoO_3$/$MoO_3$/Ag/$MoO_3$ were used; inorganic perovskite $CsPbCl_3$ was selected as the UV light absorber, and TAPC (4,4′-Cyclohexylidenebis[*N*,*N*-bis(4-methylphenyl)benzenamine]) acted as the hole transporting layer. The device area of each photonic synapse was 0.051 $cm^2$. (Figure S1, Supporting Information) Since the light illuminated from the ITO substrate side, and the thickness of $CsPbCl_3$ is thick enough to absorb all of the UV light. Therefore, there is a negligible effect of light by the top electrode. Figure 1b shows the top-view images obtained after scanning electron microscopy (SEM), and surface energy-dispersive X-ray spectroscopy (EDS) mappings are shown in Figure 1c; these images reveal the homogeneous morphology and distribution of Cs, Pb, and Cl in a vacuum-deposited perovskite thin film. In addition, the absorption spectra of $CsPbCl_3$ are shown in Figure 1d, which indicates UV-sensitive absorption. The crystallographic property of vacuum-deposited $CsPbCl_3$ was measured by X-ray diffraction (XRD) crystallography, as shown in Figure S2 (Supporting Information). Furthermore, the photoluminescence (PL) and time-resolved photoluminescence measurement were also carried out to confirm $CsPbCl_3$ thin film quality, which were shown in Figures S3 and S4 (Supporting Information).

The quantified representative synaptic functions are presented in Figure 1e–j. A 365 nm light emission diode (LED) was used as the light source to stimulate the photonic synapse device. In biological systems, critical synaptic plasticity called paired-pulse facilitation (PPF) is a short-term potentiation process essential to decode temporal information in auditory or visual signals.[37] As shown in Figure 1e, when a synapse receives two presynaptic spikes in a short time, the second postsynaptic response is enhanced, thereby causing a larger postsynaptic current (PSC) than the first one. The ratio of $A_2/A_1$ is referred to as the PPF index, where $A_1$ and $A_2$ represent the amplitude of the PSC triggered by the first and second light stimuli, respectively. Figure 1f shows the photoresponses for 10 consecutive pulses with spike intervals of 10 s. The measured results of the artificial synapse clearly exhibit PPF behavior, and the PSC increased significantly compared with the one triggered by only a single spike. Figure 1g shows the function of spike-duration dependent plasticity (SDDP), which plots PSC as a function of the spike interval. The light intensity was 12.5 μW $cm^{-2}$, and the spike duration varied between 0.5–8 s. The PPF index is 126% when the spike duration is 0.5 s, and as the pulse period extends to 8 s, the PPF index decreases to 101%. The enhanced extent is closely related to the time interval between the two spikes, and the $A_2/A_1$ decay curve with $\Delta t$ follows a double exponential function given by

$$\text{PPF index} = 1 + C_1 \cdot e^{(-\Delta t/\tau_1)} + C_2 \cdot e^{(-\Delta t/\tau_2)} \quad (1)$$

where $C_i$ and $\tau_i$ ($i$ = 1, 2) denote the initial facilitation magnitude and characteristic relaxation time, respectively. The first and second exponential terms in Equation (1) describe the rapid and slow decay processes, respectively; the originally measured data are shown in Figure S5 (Supporting Information).

Unlike SDDP, the PSC under different pulse numbers—these indicate spike-number dependent plasticity (SNDP)—were measured and the results are shown in Figure 1h. The SNDP under light intensities of 50, 25, and 12.5 μW $cm^{-2}$ are compared, and the results reveal higher PSC after consecutively increasing the pulse number. Further, the raised light intensity resulted in a larger PSC. To further identify the behaviors of photonic synapses closely related to the spike frequency, spike-frequency dependent plasticity (SFDP) was measured and the PSC was plotted as a function of pulse frequency; these values were compared with various light intensities ranging between 1.25–12.5 μW $cm^{-2}$, as shown in Figure 1i. The SFDP indices are calculated after 10 pulses of stimuli, and their peak values under different light intensities vary for different frequencies (0.1, 0.5, 1, 5, and 10 Hz; duty cycle: 50%). Further, not only frequency but also light intensity affects the maximum SFDP index. When the device was illuminated under a stronger light of 12.5 μW $cm^{-2}$, the maximum SFDP index after 10 spikes reached a considerably high value of 682.9%. Meanwhile, when

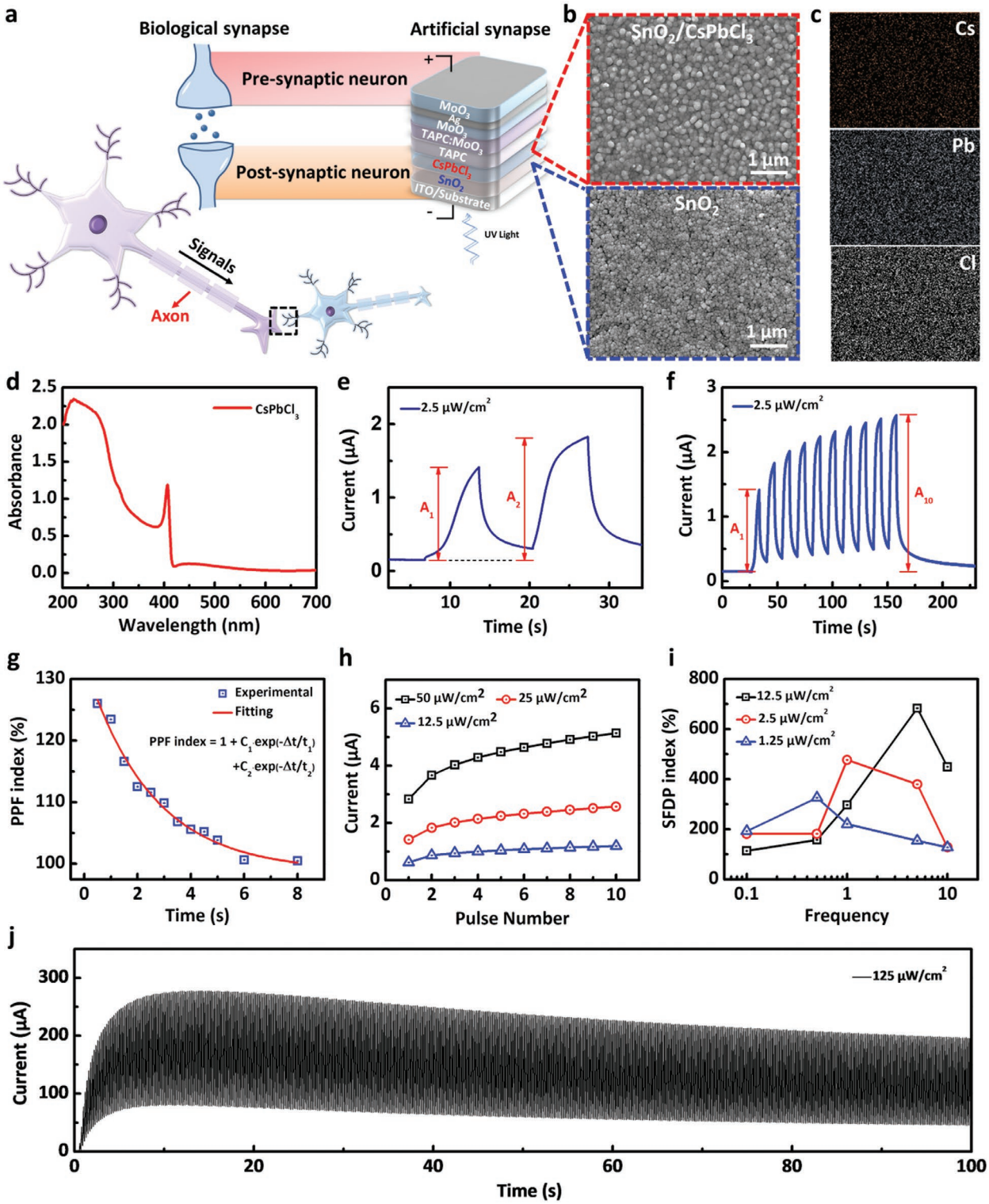


**Figure 1.** a) Schematic of biological synapse in the human brain; the synapses, neurons, and artificial two-terminal device used in this work are shown. The UV light illuminated from the ITO substrate side. b) SEM top-view images of $SnO_2$ and $CsPbCl_3$ grown on $SnO_2$. c) Cs, Pb, and Cl element distributions of vacuum-deposited $CsPbCl_3$ perovskite in an EDS (energy dispersive spectroscopy) mapping. d) Absorption spectra of the inorganic $CsPbCl_3$ perovskite. e) Representative synaptic functions used in this study; $A_1$ and $A_2$ represent the amplitudes of PSC triggered by the first and second light stimuli, respectively. The ratio of $A_2/A_1$ is defined as the PPF index. f) Photoresponse under consecutive 10 pulses with a spike interval of 10 s (0.1 Hz). The PSC increased significantly compared with the one triggered by only a single spike. g) PSC is plotted as a function of the spike interval. The light intensity was 12.5 μW $cm^{-2}$, and the spike duration varied from 0.5 to 8 s. h) Synaptic function of SNDP under various light intensities. i) SFDP index plotted as a function of frequency; the frequency ranges between 0.1–10 Hz. j) Photonic synapse device stimulated by a significantly intense UV light of 125 μW $cm^{-2}$. The measurement frequency was 10 Hz.

the device was illuminated under lights of 2.5 and 1.25 μW cm$^{-2}$, the maximum SFDP indices were 476.9% and 325.9%, respectively. In general, the SFDP index reached its maximum value at 0.5, 1, and 5 Hz under light intensities of 2.5, 1.25, and 12.5 μW cm$^{-2}$, respectively. Indeed, the $CsPbCl_3$-based synapse showed a notably high SFDP index (larger than 200%) with a peak value of 682.9%; further, it achieved an extremely sensitive photoresponse under UV light, even under a very weak 1.25 μW cm$^{-2}$ illumination. A total of 500 pulses (10 Hz) of light stimulation were applied to the photonic synapse device with a more intensive UV light intensity of 125 μW cm$^{-2}$, as shown in Figure 1j. Under this condition, the synaptic current increased at the beginning and gradually dropped after ≈50 pulses. This neuromorphic characteristic mimics the behavior of the human iris to control the amount of incoming light in various light environments.[38,39] When synapse devices are illuminated under intense light—analogous to intensive light entering the iris—the PSC readjusts accordingly. This unique property of the biological photonic synapse can potentially be utilized in some auto-adjustment machines. The device behavior under various stimulated light frequencies (1–1000 Hz) is shown in Figure S6 (Supporting Information).

A typical learning and memory model of a human brain originally proposed by Atkinson and Shiffrin[40] for short- and long-term memory is illustrated in **Figure 2**a. According to this model, new memories are transiently encoded into a temporary store in the hippocampus as a short-term memory. These memories are either gradually transferred into a long-term store (represented by the neocortex) or discarded. Short-term potentiation (STP) and long-term potentiation (LTP) are distinguished based on their retention times, wherein STP lasts for tens of milliseconds and LTP lasts for minutes.[41] Synapse plasticity, which is the strength of the connection between a pre- and post-neuron, is believed to be the basis of memory function of the brain. Figure 2b demonstrates the dependence of measured current on light intensity and light illumination time in the human visual memory simulated by the artificial optical synapses. The optical image of the artificial synapse device when it was measuring with UV light is shown in Figure S7 (Supporting Information). The 3 × 3 pixels device and the photograph of "U" shape light signal are shown in Figure S8 (Supporting Information). Figure S9 (Supporting Information) presents the readout circuit of the array. We stimulated the photonic artificial devices under different light intensities ranging between 1.25–25 μW cm$^{-2}$ with light illumination time up to 5 s. The input images in the letter "U" comprised 3 × 3 pixels encoded by various light intensities and light illumination time. The measured currents were shown on each pixel in Figure 2b, and the impact of stimulated light intensity and stimulation time on artificial optical synapses could be easily compared from the figure. Under dimmer light conditions of 1.25 and 2.5 μW cm$^{-2}$, the measured current of each device after 5 s was 0.45 and 1.13 μA, respectively. These PSCs were obvious smaller, which indicated a smaller synapse plasticity. At a light intensity of 12.5 and 25 μW cm$^{-2}$, the PSCs after 5 s of UV light illumination increased to 12.9 and 33.1 μA, respectively. The PSC enlarged gradually with the prolonged light illumination time, which showed an enhanced memory with the increased time of UV light illumination. In biological neuron networks, the larger stimulation, the stronger link between neurons, which is well corresponding to the measurement results of our photonic artificial synapse devices. The regulation of synapse plasticity presented the ability to control the photo-recording functionality, which mimics the biological memory system and learning behavior.[11]

Based on the above data, we suspect that the synaptic characteristics (PPF, SDDP, SNDP, SFDP, STP, and LTP) of our optical artificial synapse devices are attributed to UV light-induced trapping/detrapping of carriers at the $SnO_2$ and $CsPbCl_3$ perovskite interface, as illustrated in **Figure 3**. The light-induced change in conductivity is called "photogating,"[42] which is a concept previously used in transistor-based flash memories.[22] Figure 3a shows the band diagram of $SnO_2$/$CsPbCl_3$ in the dark condition, and this energy-level diagram is determined using ultraviolet photoelectron spectroscopy (UPS) measurement (Figure S10, Supporting Information). The band alignment between $SnO_2$ and $CsPbCl_3$ heterostructure leads to the separation of excitons in the interface, which serves as the basis for optically mediated charge trapping in $CsPbCl_3$-based artificial synapses.[43] Under UV light illumination and reverse bias, the band diagram bends[44] as implied in Figure 3b. The synapse behaviors are attributed to the transition from direct to Fowler–Nordheim (F–N) tunneling[16,45,46] as shown in Figure 3c. When applying the reverse bias, the electrons tunnel from $CsPbCl_3$ through $SnO_2$. After the removal of the light stimuli, the current exhibits a rapid drop because of the band-to-band transition;[47] the PSC value does not return to its initial state; and the trapped electrons in $SnO_2$/$CsPbCl_3$ interface are retained for a long time because of the trapping energy barrier that leads to a change in conductance level, which increases the PSC value. As the reverse bias increases under UV light illumination, there is an obviously inflection point at ≈–0.36 V in the $\ln(I/V^2)$ versus $1/V$ plot. In contrast, the slope of $\ln(I/V^2)$ versus $1/V$ plot at the reverse bias in the dark is close to linear, as shown in Figure S11 (Supporting Information).

This phenomenon indicated that synapse behavior occurs at a reverse bias larger than –0.36 V. The $I$–$V$ characteristics of the photonic synapse for 10 loops are obtained as shown in Figure 3d. The current values for the 10 loops remain the same before –0.36 V; however, they gradually increase with the loop for a bias greater than –0.36 V. The numbers (1) to (10) in Figure 3d represents the ordinal number of the loops. The data confirm that the charge carrier transport is dominated by F–N tunneling at a reverse bias larger than –0.36 V, and thus, it causes photonic synapse behaviors. Figure 3e shows the PSC of the photonic artificial device under a light intensity of 50 μW cm$^{-2}$. Note that not only the photocurrent but also the dark current increase gradually, which clearly reveals the trap filling process induced by the light-introduced charges. The photosensitive performance of the synapse device is investigated by adding a $C_{60}$ layer between $SnO_2$ and the $CsPbCl_3$ perovskite to confirm the interfacial charge trapping effect. As shown in Figure 3f, with an increased thickness of $C_{60}$ (from 0–10 nm), the photoresponse current becomes considerably smaller, and the synaptic behavior gradually disappears. Further, the increased thickness of $C_{60}$ (from 50–200 nm) is depicted in Figure S12 (Supporting Information). The results indicate

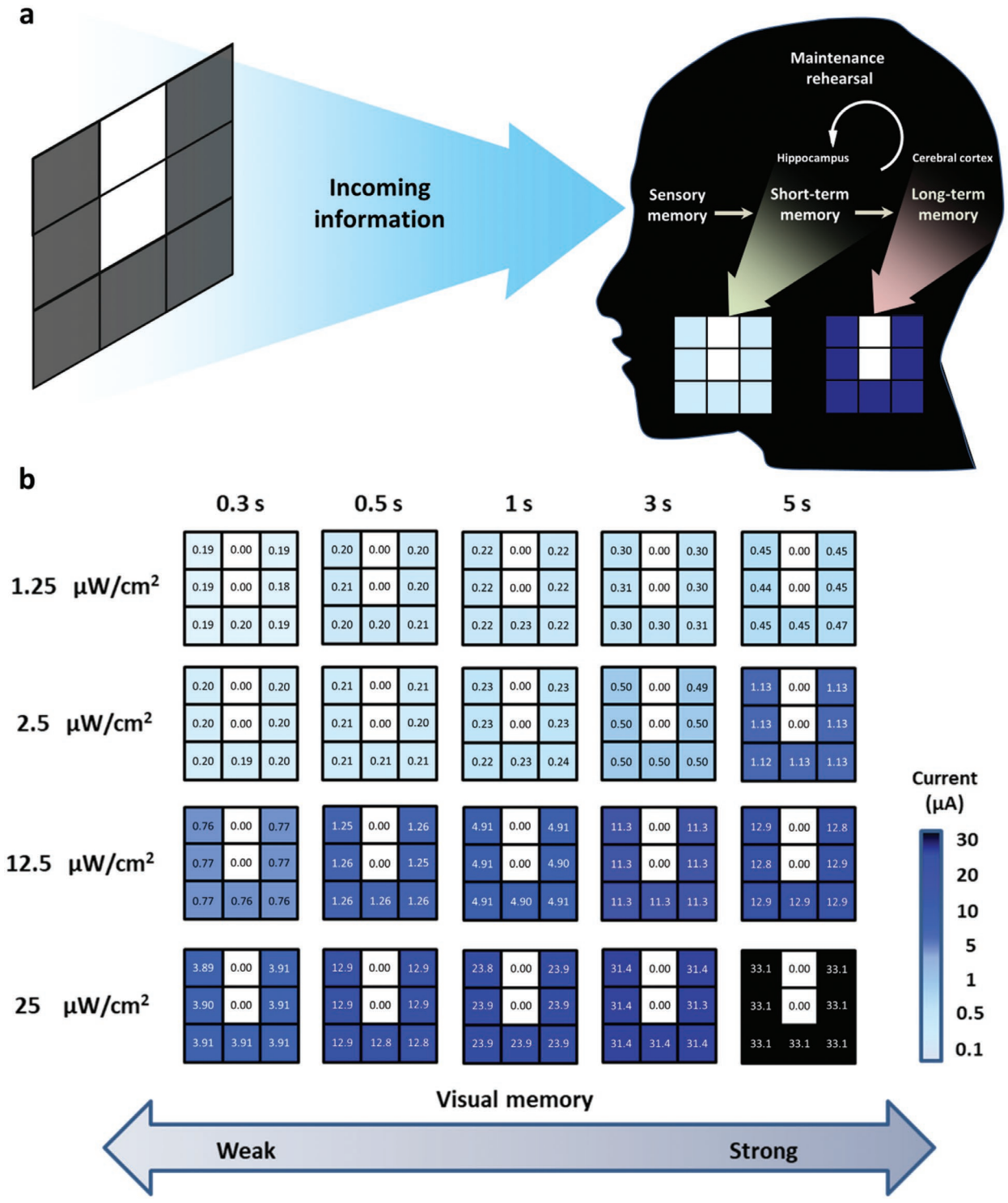


**Figure 2.** a) Typical learning and memory model of a human brain using short-term and long-term memories. New memories are transiently encoded into a temporary store in the hippocampus as short-term memories. b) The input images in the letter "U" consist of 3 × 3 pixels encoded by various light intensities and light illumination time. The number in each pixel is the measured PSC value.

that the increased thickness of $C_{60}$ leads to a reduction of the photoinduced trap states between the $SnO_2$/$CsPbCl_3$ interface, which weakens the interfacial effect and reconfirms the abovementioned mechanism.

With the advantages of the layer-by-layer vacuum deposition, the dielectric/metal/dielectric (DMD) transparent flexible electrode structure and flexible substrate are incorporated to enforce devices with transparency and flexibility.[48,49] In the

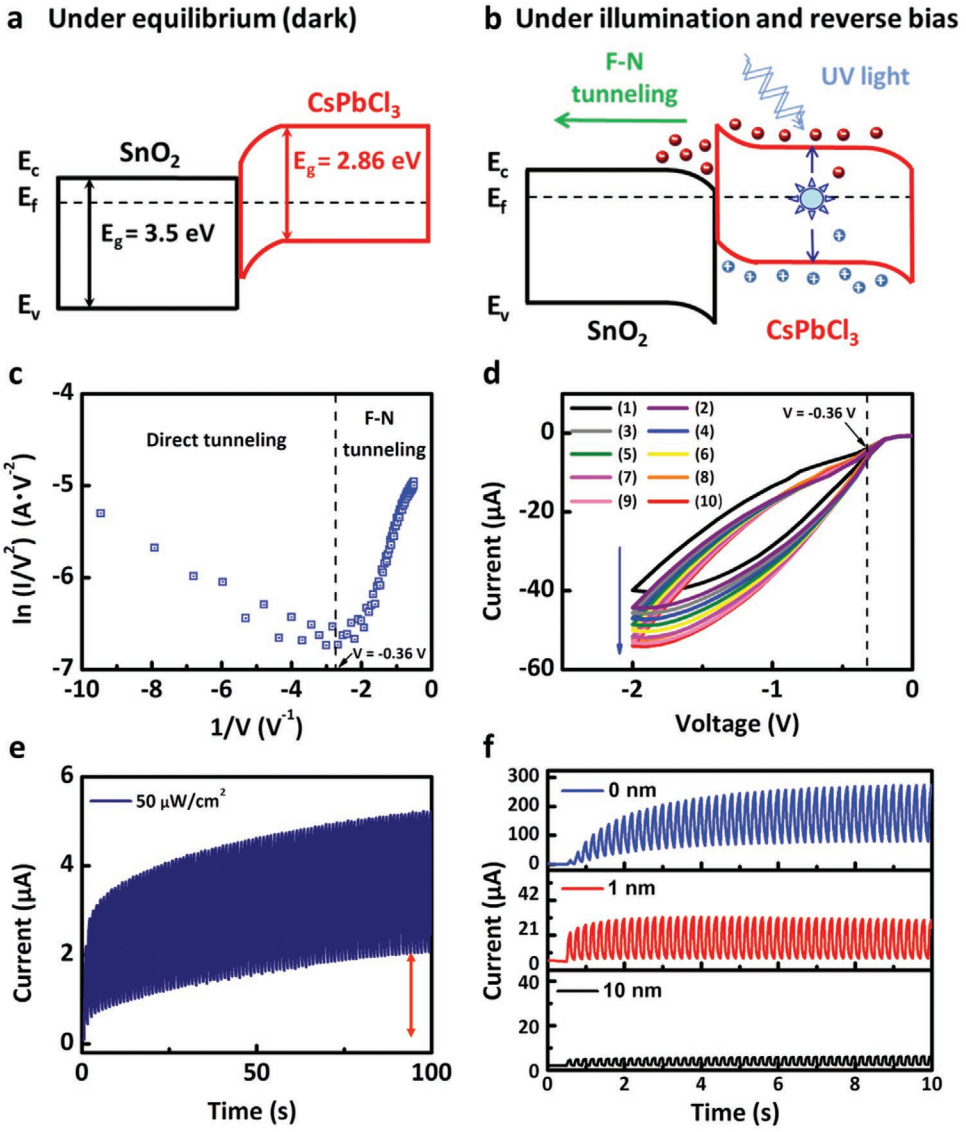


**Figure 3.** Contributing mechanism for the observed synaptic behavior. a) Band diagram under thermal equilibrium (dark). b) After UV light illumination, electrons transport through $SnO_2$ by F–N tunneling under reverse bias, and some of them are trapped at the $SnO_2$/$CsPbCl_3$ interface after the removal of light, thereby leading to a change in the conductance level. c) The $\ln(I/V^2)$ versus $1/V$ plot under UV light illumination. An inflection point at –0.36 V implies the transformation from direct tunneling to F–N tunneling. d) The *I–V* characteristic curve after 10 loops of scanning under UV light illumination. The numbers (1) to (10) represents the ordinal numbers of the loops, and the currents after UV light stimuli were obviously enhanced by the increased cycle of loops. e) Optical synaptic currents under the light intensity of 50 μW $cm^{-2}$. The double arrow sign shows the increased dark current after UV light spikes, which clearly reveals the trap filling process using the photogenerated e–h pairs. f) The PSC measurement of the artificial synapse devices includes different thicknesses of the $C_{60}$ layer between $SnO_2$ and $CsPbCl_3$. A thicker $C_{60}$ layer yields a considerably smaller current; the measurement parameters are controlled at 10 Hz.

DMD structures, the structure thicknesses and materials are designed judiciously for maximum broadband transmission, and the DMD layers provide only suitable optical resonance structures without altering the electrical properties of the devices.[50] The optimized thickness of each layer is fine-tuned using an in-house panchromatic optical field simulation program.[48,49] The optical artificial synapse devices with a structure of ITO/$SnO_2$/$CsPbCl_3$/TAPC/TAPC:$MoO_3$/$MoO_3$/Ag/$MoO_3$ are demonstrated, as illustrated previously in Figure 1b. Furthermore, several types of substrates including glass, flexible PET, and Parylene-C are verified. **Figure 4**a,b and Figure S13 (Supporting Information) show the photographs of transparent devices with bending capability. The full-device transmission spectra are shown in Figure S14 (Supporting Information).

The excellent charge transport properties of TAPC doped with conductive dopant ($MoO_3$) films were previously used in organic photovoltaics and perovskite solar cells.[51] In addition, the TAPC:$MoO_3$ films exhibit an absorption in the deep red to near-infrared (NIR) wavelength, which corresponds to the charge-transfer states between TAPC molecules and $MoO_3$ dopants. This unique characteristic allows devices to achieve visible transparency while exhibiting a deep red to NIR

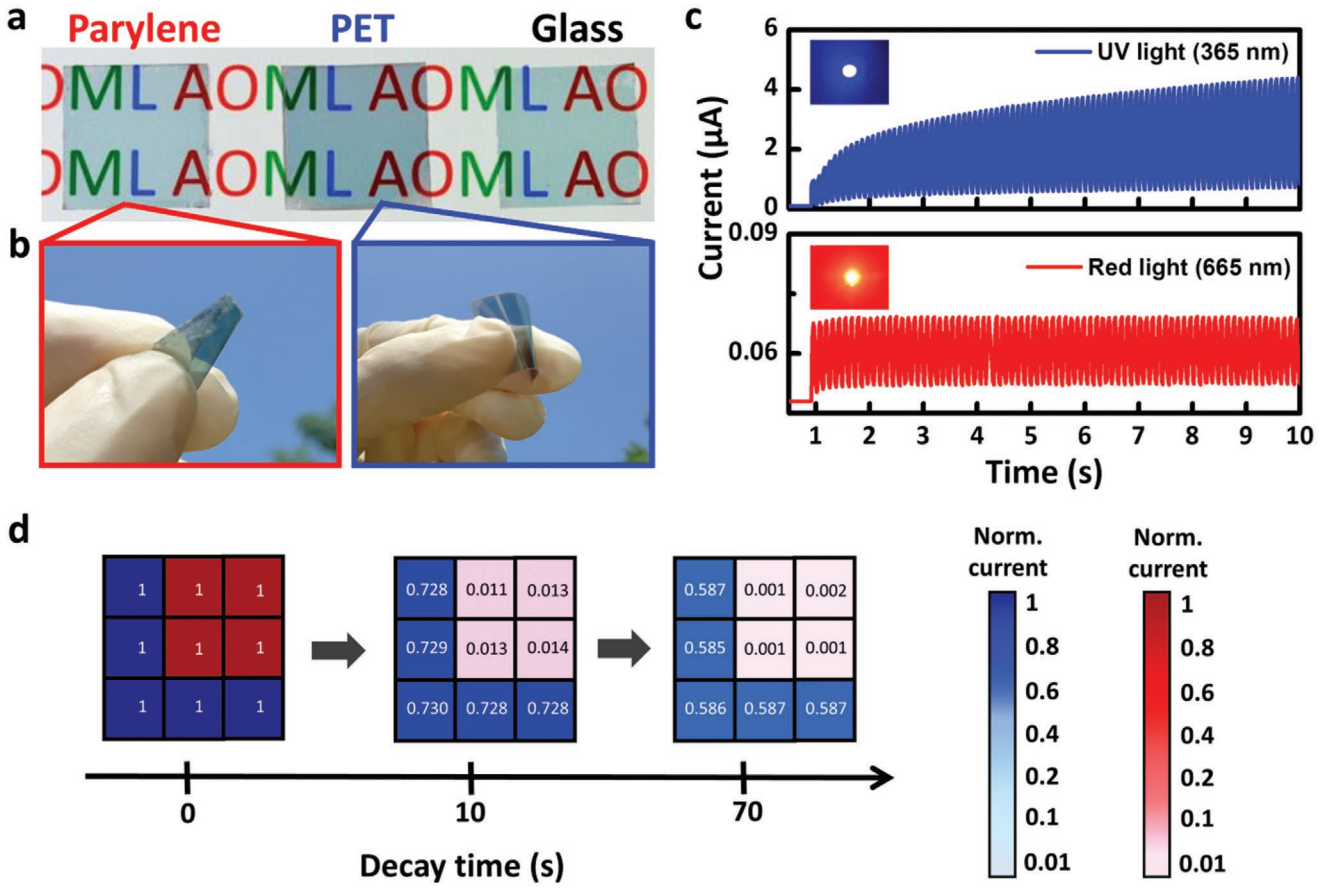


**Figure 4.** a) We verified highly transparent artificial synapse devices on three types of substrates including Parylene-C (5 μm), PET (0.25 mm), and glass (1 mm). The photograph shows these substrates placed on a smart phone with letters "AOML" onside. b) Photograph of the flexible and high transparence artificial photonic devices of PET and Parylene-C substrates under the blue sky. c) Extinction coefficient absorption at a peak of 685 nm of TAPC-doped $MoO_3$ thin film allows dual-mode operation under deep-red light (665 nm) for the artificial synapse, which distinguishes the behavior under UV light (365 nm). The measurement frequency was 10 Hz. d) With predefined pixel colors (UV and red light) and light intensity, the decay measurement was performed for a fixed period of 70 s after 10 s stimulation (10 Hz) was removed. PSCs under UV and red light stimulations were normalized, respectively. The number in each pixel was the normalized PSC value. Illumination in only UV light resulted in long-term memory, and it formed the shape of the letter "L". The different behavior in the same device structure with a transparent appearance enables image detection and recognition using a different light color.

photoresponse. As shown in Figure 4c, the device showed a clear photoresponse to deep red light. However, unlike the UV-light stimulated synaptic behavior, the highest photocurrent did not increase with repeated red light illumination, which indicates that no memory behavior can occur even under continuous rehearsal. Because the red light does not cause photocarrier generation in $CsPbCl_3$ (similar to $CsPbCl_3$ in dark), it does not trigger the photocarrier trapped/de-trapped process, thereby resulting in no synaptic behavior. As a consequence, the photonic artificial synapses exhibited very different photoresponse behaviors to the UV and deep red light stimulations. To provide the proof-of-concept for this dual-mode photonic operation, the following experiment was conducted. First, we randomly chose nine photonic synapse devices from the same batch. After illumination at 10 Hz under different light colors, 3 × 3 pixels were encoded by the PSC values of these devices. The stimuli of lights were removed after 10 s, and we normalized the PSC values of UV and red light, respectively. Because of the various PSC decay rates, 3 × 3 pixels finally formed a shape like the letter "L". 365 and 665 nm LEDs were utilized as light sources to stimulate the device. For a fixed period of 70 s, we can clearly differentiate the photonic information from the remaining PSC for the first several seconds, as presented in Figure 4d. The synapse devices under red light illumination do not have memory capabilities; however, devices stimulated with UV light have a long-term memory greater than 70 s, which mimics the biological visual memory function. The dual-mode operation synapse device enables image detection and recognition under different light colors.

## 3. Conclusion

In conclusion, we demonstrated the first implementation of UV-absorbing inorganic perovskite $CsPbCl_3$ in photonic artificial synapses, which exhibit the necessary synaptic functions of PPF, SDDP, SNDP, and SFDP. Other important neuromorphic characteristics of STP and LTP, serving as biological human

short-term memory and long-term memory, were also attained. Additionally, different synaptic behaviors under various light intensities and frequencies were carefully compared, and long-term synaptic plasticity was preliminarily achieved through repeated light pulses. Electron trapping and detrapping at the interface of $SnO_2$/$CsPbCl_3$ enabled the characteristic of consecutive changes in photoconductivity. Furthermore, transparent and flexible photonic synapse devices with a DMD structure were obtained. Finally, the additional charge-transfer absorption of TAPC doped $MoO_3$ film enabled the transparent appearance of the device while exhibiting a dual-mode operation under UV and red light. This study demonstrated a novel device architecture and fabrication method for inorganic perovskite photonic artificial synapses. The two-terminal device architecture is not only closer to the structure of a biological synapse, but also enables high transparency and flexibility, which can help facilitate higher integration density in 3D stacking memristors. With the functionality mimicking human memory behavior, we are deeply convinced that based on the architecture established in this work, these versatile synaptic functionalities open up a new era of flexible and transparent perovskite artificial synapses for optically controllable multilevel data storage, pattern recognition, and bio-inspired smart artificial visual devices.

## 4. Experimental Section

*Device Fabrication*: Patterned indium tin oxide (ITO) substrates (145 nm, Nichem) were cleaned with detergent, deionized (DI) water, acetone, and methanol in sequence, and they were then treated with ultraviolet ozone (UVO) for 15 min for further cleaning. The $SnO_2$ nanoparticles were sonicated 20 min prior to being spin coated (3000 rpm, 30 s) on the ITO substrate.[52] The substrates were then transferred to a high-vacuum chamber (base pressure of $\approx 2 \times 10^{-6}$ Torr) to deposit perovskite. The perovskite layer was co-deposited along with CsCl:$PbCl_2$ at a 1:1 molar ratio. Further, CsCl was deposited at a rate of 0.8 Å $s^{-1}$, whereas $PbCl_2$ was deposited at a rate of 0.9 Å $s^{-1}$. During the co-deposition, the deposition rates were monitored using three quartz crystal microbalance sensors. The first sensor monitored the deposition rate of the cesium halides; the second, the deposition rate of the lead halide; and the third, the total co-deposition rate on the sample. After co-deposition, the samples were transferred to a nitrogen glove box and annealed at 120 °C for 5 min.[31] After thermal annealing, the samples were loaded back to a high-vacuum chamber (base pressure of $<2 \times 10^{-6}$ Torr) for 4,4′-Cyclohexylidenebis[*N*,*N*-bis(4-methylphenyl) benzenamine] (TAPC), TAPC:$MoO_3$ (65:35, v/v), $MoO_3$, and Ag depositions. Finally, highly transparent devices that exhibited a structure of ITO (145 nm)/$SnO_2$ (10 nm)/$CsPbCl_3$ (150 nm)/TAPC (20 nm)/TAPC:$MoO_3$ (90 nm)/$MoO_3$ (10 nm)/Ag (12.5 nm)/$MoO_3$ (40 nm) were fabricated. The thicknesses of the Parylene-C and PET substrates were 5 µm and 0.25 mm, respectively. The thickness of the ITO was 100 nm on Parylene-C and PET. The area of each sample was 0.051 $cm^2$ or 1 $mm^2$, and it was defined by shadow masks.

*Optical Simulation and Optimization*: A self-made panchromatic optical field simulation program based on a transfer matrix method was utilized to model the optical field distribution; the program was coded in MATLAB (R2010a). The layer thickness and wavelength-dependent complex optical constants of each layer required in the simulation were carefully acquired for each wavelength using VASE (J.A. Woollam).

*Device Measurement and Characterization*: $CsPbCl_3$ perovskite thin films for absorption were directly prepared on the fused quartz substrate. The SEM measurements used the glass substrate/ITO (145 nm)/$CsPbCl_3$ (150 nm) structure. The absorption and transmission spectra were acquired using a Shimadzu UV-2600 UV–vis spectrophotometer; the SEM images were obtained using a JSM-7000F scanning electron microscope. The X-ray diffractions were conducted using a Bruker D2 phaser with Cu$K\alpha$ radiation. The PL spectra were detected in a front-face configuration using a fiber-based spectrograph coupled with a charge-coupled device (CCD) camera (PIXIS256BR, Princeton Instruments), and a stable diode laser ($\lambda = 375$ nm) as the pumping source. A 365 nm LED (Thorlabs) was used as the light stimulation source. The intensity of the 365 nm LED was calibrated using an NIST-traceable Ophir power meter. For the frequency ranging between 0.1–5 Hz, the photocurrent of the synapse device was recorded using a Keithley SourceMeter 2636B. For a frequency larger than 5 Hz, the measurements were performed using a Keysight B1500 semiconductor parameter analyzer. For the UPS measurement, the valance-band UV photoemission spectra were obtained using HeI (21.2 eV) as the excitation source, and photoemitted electrons were counted using a hemispherical analyzer with an overall resolution of 0.05 eV. The absolute energy scale of the UPS profile is relative to the Fermi edge, and the 4f core level of a sputter-cleaned gold substrate, respectively. To eliminate the analyzer effect, a sample bias of −5 eV was applied when acquiring the secondary electron cutoff spectra.

## Supporting Information

Supporting Information is available from the Wiley Online Library or from the author.

## Acknowledgements

The authors would like to acknowledge the financial support from the Ministry of Science and Technology of Taiwan (Grant Nos. 109-2636-E-007-009 and 109-2634-F-007-023, respectively); Academia Sinica (Grant Nos. AS-SS-109-05); and "Frontier Research Center on Fundamental and Applied Sciences of Matters" from The Featured Areas Research Center Program within the framework of the Higher Education Sprout Project by the Ministry of Education (MOE) in Taiwan.

## Conflict of Interest

The authors declare no conflict of interest.

## Keywords

artificial synapses, dual-mode operation, inorganic perovskites, photonic memristors, transparent devices

Received: September 28, 2020
Revised: October 21, 2020
Published online:

[1] F. Peper, *New Gener. Comput.* **2017**, *35*, 253.
[2] S. Choi, S. Jang, J. H. Moon, J. C. Kim, H. Y. Jeong, P. Jang, K. J. Lee, G. Wang, *NPG Asia Mater.* **2018**, *10*, 1097.
[3] Z. Wang, S. Joshi, S. E. Savel'ev, H. Jiang, R. Midya, P. Lin, M. Hu, N. Ge, J. P. Strachan, Z. Li, Q. Wu, M. Barnell, G. L. Li, H. L. Xin, R. S. Williams, Q. Xia, J. J. Yang, *Nat. Mater.* **2017**, *16*, 101.
[4] M. L. Schneider, C. A. Donnelly, S. E. Russek, B. Baek, M. R. Pufall, P. F. Hopkins, P. D. Dresselhaus, S. P. Benz, W. H. Rippard, *Sci. Adv.* **2018**, *4*, 1701329.
[5] T. Ahmed, S. Kuriakose, E. L. H. Mayes, R. Ramanathan, V. Bansal, M. Bhaskaran, S. Sriram, S. Walia, *Small* **2019**, *15*, 1900966.

[6] Y. van de Burgt, E. Lubberman, E. J. Fuller, S. T. Keene, G. C. Faria, S. Agarwal, M. J. Marinella, A. Alec Talin, A. Salleo, *Nat. Mater.* **2017**, *16*, 414.
[7] W. Xu, H. Cho, Y. H. Kim, Y. T. Kim, C. Wolf, C. G. Park, T. W. Lee, *Adv. Mater.* **2016**, *28*, 5916.
[8] Y. Y. Shi, X. H. Liang, B. Yuan, V. Chen, H. T. Li, F. Hui, Z. C. W. Yu, F. Yuan, E. Pop, H. S. P. Wong, M. Lanza, *Nat. Electron.* **2018**, *1*, 458.
[9] S. Ham, S. Choi, H. Cho, S. I. Na, G. Wang, *Adv. Funct. Mater.* **2019**, *29*, 1806646.
[10] J. Feldmann, N. Youngblood, C. D. Wright, H. Bhaskaran, W. H. P. Pernice, *Nature* **2019**, *569*, 208.
[11] H. L. Park, H. Kim, D. Lim, H. Zhou, Y. H. Kim, Y. Lee, S. Park, T. W. Lee, *Adv. Mater.* **2020**, *32*, 1906899.
[12] H. Wang, Q. Zhao, Z. Ni, Q. Li, H. Liu, Y. Yang, L. Wang, Y. Ran, Y. Guo, W. Hu, Y. Liu, *Adv. Mater.* **2018**, *30*, 1803961.
[13] B. Pradhan, S. Das, J. Li, F. Chowdhury, J. Cherusseri, D. Pandey, D. Dev, A. Krishnaprasad, E. Barrios, A. Towers, A. Gesquiere, L. Tetard, T. Roy, J. Thomas, *Sci. Adv.* **2020**, *6*, eaay5225.
[14] Z. Y. Lv, M. Chen, F. S. Qian, V. A. L. Roy, W. B. Ye, D. H. She, Y. Wang, Z. X. Xu, Y. Zhou, S. T. Han, *Adv. Funct. Mater.* **2019**, *29*, 1902374.
[15] Y. L. Sun, L. Qian, D. Xie, Y. X. Lin, M. X. Sun, W. W. Li, L. M. Ding, T. L. Ren, T. Palacios, *Adv. Funct. Mater.* **2019**, *29*, 1902538.
[16] M. Kumar, S. Abbas, J. Kim, *ACS Appl. Mater. Interfaces* **2018**, *10*, 34370.
[17] S. Chen, Z. Lou, D. Chen, G. Shen, *Adv. Mater.* **2018**, *30*, 1705400.
[18] F. M. Ma, Y. B. Zhu, Z. W. Xu, Y. Liu, X. J. Zheng, S. Ju, Q. Q. Li, Z. Q. Ni, H. L. Hu, Y. Chai, C. X. Wu, T. W. Kim, F. S. Li, *Adv. Funct. Mater.* **2020**, *30*, 1908901.
[19] D. Hao, J. Zhang, S. Dai, J. Zhang, J. Huang, *ACS Appl. Mater. Interfaces* **2020**, *12*, 39487.
[20] Y. Wang, Z. Lv, J. Chen, Z. Wang, Y. Zhou, L. Zhou, X. Chen, S. T. Han, *Adv. Mater.* **2018**, *30*, 1802883.
[21] D. C. Hu, R. Yang, L. Jiang, X. Guo, *ACS Appl. Mater. Interfaces* **2018**, *10*, 6463.
[22] J. Y. Mao, L. Zhou, X. J. Zhu, Y. Zhou, S. T. Han, *Adv. Opt. Mater.* **2019**, *7*, 1900766.
[23] R. Rosezin, E. Linn, L. Nielen, C. Kugeler, R. Bruchhaus, R. Waser, *IEEE Electron Device Lett.* **2011**, *32*, 191.
[24] M. Prezioso, F. Merrikh-Bayat, B. D. Hoskins, G. C. Adam, K. K. Likharev, D. B. Strukov, *Nature* **2015**, *521*, 61.
[25] R. Robucci, J. D. Gray, L. K. Chiu, J. Romberg, P. Hasler, *Proc. IEEE* **2010**, *98*, 1089.
[26] C. Wu, T. W. Kim, H. Y. Choi, D. B. Strukov, J. J. Yang, *Nat. Commun.* **2017**, *8*, 752.
[27] D. Berco, D. Shenp Ang, *Adv. Intell. Syst.* **2019**, *1*, 1900003.
[28] V. Daneault, M. Hebért, G. Albouy, J. Doyon, M. Dumont, J. Carrier, G. Vandewalle, *Sleep* **2014**, *37*, 85.
[29] G. Vandewalle, C. Schmidt, G. Albouy, V. Sterpenich, A. Darsaud, G. Rauchs, P. Y. Berken, E. Balteau, C. Degueldre, A. Luxen, P. Maquet, D. J. Dijk, *PLoS One* **2007**, *2*, 1247.
[30] G. Vandewalle, O. Collignon, J. T. Hull, V. Daneault, G. Albouy, F. Lepore, C. Phillips, J. Doyon, C. A. Czeisler, M. Dumont, S. W. Lockley, J. Carrier, *J. Cognit. Neurosci.* **2013**, *25*, 2072.
[31] L. Yang, W. L. Tsai, C. S. Li, B. W. Hsu, C. Y. Chen, C. I. Wu, H. W. Lin, *ACS Appl. Mater. Interfaces* **2019**, *11*, 47054.
[32] Y. Fujii, S. Hoshino, Y. Yamada, G. Shirane, *Phys. Rev. B* **1974**, *9*, 4549.
[33] Z. Li, Z. Chen, Y. Yang, Q. Xue, H. L. Yip, Y. Cao, *Nat. Commun.* **2019**, *10*, 1027.
[34] Y. Chen, W. J. Qiu, X. W. Wang, W. R. Liu, J. X. Wang, G. Z. Dai, Y. B. Yuan, Y. L. Gao, J. Sun, *Nano Energy* **2019**, *62*, 393.
[35] M. Kumar, H. S. Kim, J. Kim, *Adv. Mater.* **2019**, *31*, 1900021.
[36] S. Gao, G. Liu, H. Yang, C. Hu, Q. Chen, G. Gong, W. Xue, X. Yi, J. Shang, R. W. Li, *ACS Nano* **2019**, *13*, 2634.
[37] G. Wu, P. Feng, X. Wan, L. Zhu, Y. Shi, Q. Wan, *Sci. Rep.* **2016**, *6*, 23578.
[38] L. Zhao, Z. Fan, S. Cheng, L. Hong, Y. Li, G. Tian, D. Chen, Z. Hou, M. Qin, M. Zeng, X. Lu, G. Zhou, X. Gao, J. M. Liu, *Adv. Electron. Mater.* **2020**, *6*, 1900858.
[39] G. J. Lee, C. Choi, D. H. Kim, Y. M. Song, *Adv. Funct. Mater.* **2018**, *28*, 1705202.
[40] R. M. Shiffrin, R. C. Atkinson, *Psychol. Rev.* **1969**, *76*, 179.
[41] J. Born, I. Wilhelm, *Psychol. Res.* **2012**, *76*, 192.
[42] H. Fang, W. Hu, *Adv. Sci.* **2017**, *4*, 1700323.
[43] J. Lee, S. Pak, Y. W. Lee, Y. Cho, J. Hong, P. Giraud, H. S. Shin, S. M. Morris, J. I. Sohn, S. Cha, J. M. Kim, *Nat. Commun.* **2017**, *8*, 14734.
[44] F. Wu, B. Bahrami, K. Chen, S. Mabrouk, R. Pathak, Y. Tong, X. Li, T. Zhang, R. Jian, Q. Qiao, *ACS Appl. Mater. Interfaces* **2018**, *10*, 25604.
[45] X. B. Yan, L. Zhang, H. W. Chen, X. Y. Li, J. J. Wang, Q. Liu, C. Lu, J. S. Chen, H. Q. Wu, P. Zhou, *Adv. Funct. Mater.* **2018**, *28*, 1803728.
[46] X. B. Yan, J. H. Zhao, S. Liu, Z. Y. Zhou, Q. Liu, J. S. Chen, X. Y. Liu, *Adv. Funct. Mater.* **2018**, *28*, 1705320.
[47] H. K. He, R. Yang, W. Zhou, H. M. Huang, J. Xiong, L. Gan, T. Y. Zhai, X. Guo, *Small* **2018**, *14*, 1800079.
[48] W. L. Tsai, C. Y. Chen, Y. T. Wen, L. Yang, Y. L. Cheng, H. W. Lin, *Adv. Mater.* **2019**, *31*, 1900231.
[49] Y. H. Chen, C. W. Chen, Z. Y. Huang, W. C. Lin, L. Y. Lin, F. Lin, K. T. Wong, H. W. Lin, *Adv. Mater.* **2014**, *26*, 1129.
[50] X. Guo, X. Liu, F. Lin, H. Li, Y. Fan, N. Zhang, *Sci. Rep.* **2015**, *5*, 10569.
[51] Y. H. Chen, C. W. Chen, Z. Y. Huang, K. T. Wong, L. Y. Lin, F. Lin, H. W. Lin, *Org. Electron.* **2014**, *15*, 1828.
[52] M. Singh, A. Ng, Z. Ren, H. Hu, H.-C. Lin, C.-W. Chu, G. Li, *Nano Energy* **2019**, *60*, 275.